

Pulsating hydrogen-deficient white dwarfs and pre-white dwarfs observed with TESS

III. Asteroseismology of the DBV star GD 358

A. H. Córscico^{1,2}, M. Uzundag^{3,4}, S. O. Kepler⁵, R. Silvotti⁶, L. G. Althaus^{1,2}, D. Koester⁷, A. S. Baran^{8,9,10}, K. J. Bell^{11,*}, A. Bischoff-Kim¹², J. J. Hermes¹³, S. D. Kawaler¹⁴, J. L. Provencal^{15,16}, D. E. Winget^{17,18}, M. H. Montgomery^{17,18}, P. A. Bradley¹⁹, S. J. Kleinman²⁰, and A. Nitta²⁰

¹ Grupo de Evolución Estelar y Pulsaciones. Facultad de Ciencias Astronómicas y Geofísicas, Universidad Nacional de La Plata, Paseo del Bosque s/n, 1900 La Plata, Argentina

e-mail: acorsico@fcaglp.unlp.edu.ar

² IALP – CONICET, La Plata, Argentina

³ Instituto de Física y Astronomía, Universidad de Valparaíso, Gran Bretaña 1111, Playa Ancha, Valparaíso 2360102, Chile

⁴ European Southern Observatory, Alonso de Cordova 3107, Santiago, Chile

⁵ Instituto de Física, Universidade Federal do Rio Grande do Sul, 91501-970 Porto-Alegre, RS, Brazil

⁶ INAF-Osservatorio Astrofisico di Torino, strada dell'Osservatorio 20, 10025 Pino Torinese, Italy

⁷ Institut für Theoretische Physik und Astrophysik, Universität Kiel, 24098 Kiel, Germany

⁸ ARDASTELLA Research Group, Institute of Physics, Pedagogical University of Krakow, ul. Podchorążych 2, 30-084 Kraków, Poland

⁹ Embry-Riddle Aeronautical University, Department of Physical Science, Daytona Beach, FL 32114, USA

¹⁰ Department of Physics, Astronomy, and Materials Science, Missouri State University, Springfield, MO 65897, USA

¹¹ DIRAC Institute, Department of Astronomy, University of Washington, Seattle, WA 98195, USA

¹² Penn State Worthington Scranton, Dunmore, PA 18512, USA

¹³ Department of Astronomy, Boston University, Boston, MA 02215, USA

¹⁴ Department of Physics and Astronomy, Iowa State University, Ames, IA 50011, USA

¹⁵ University of Delaware, Department of Physics and Astronomy Newark, DE 19716, USA

¹⁶ Delaware Asteroseismic Research Center, Mt. Cuba Observatory, Greenville, DE 19807, USA

¹⁷ Department of Astronomy, University of Texas at Austin, Austin, TX 78712, USA

¹⁸ McDonald Observatory, Fort Davis, TX 79734, USA

¹⁹ XCP-6, MS F-699 Los Alamos National Laboratory, Los Alamos, NM 87545, USA

²⁰ Gemini Observatory/NSF's NOIRLab, 670 N. A'ohoku Place, Hilo, HI 96720, USA

Received 3 September 2021 / Accepted 30 November 2021

ABSTRACT

Context. The collection of high-quality photometric data by space telescopes, such as the completed *Kepler* mission and the ongoing TESS program, is revolutionizing the area of white-dwarf asteroseismology. Among the different kinds of pulsating white dwarfs, there are those that have He-rich atmospheres, and they are called DBVs or V777 Her variable stars. The archetype of these pulsating white dwarfs, GD 358, is the focus of the present paper.

Aims. We report a thorough asteroseismological analysis of the DBV star GD 358 (TIC 219074038) based on new high-precision photometric data gathered by the TESS space mission combined with data taken from the Earth.

Methods. We reduced TESS observations of the DBV star GD 358 and performed a detailed asteroseismological analysis using fully evolutionary DB white-dwarf models computed accounting for the complete prior evolution of their progenitors. We assessed the mass of this star by comparing the measured mean period separation with the theoretical averaged period spacings of the models, and we used the observed individual periods to look for a seismological stellar model. We detected potential frequency multiplets for GD 358, which we used to identify the harmonic degree (ℓ) of the pulsation modes and rotation period.

Results. In total, we detected 26 periodicities from the TESS light curve of this DBV star using standard pre-whitening. The oscillation frequencies are associated with nonradial g (gravity)-mode pulsations with periods from \sim 422 s to \sim 1087 s. Moreover, we detected eight combination frequencies between \sim 543 s and \sim 295 s. We combined these data with a huge amount of observations from the ground. We found a constant period spacing of 39.25 ± 0.17 s, which helped us to infer its mass ($M_\star = 0.588 \pm 0.024 M_\odot$) and constrain the harmonic degree ℓ of the modes. We carried out a period-fit analysis on GD 358, and we were successful in finding an asteroseismological model with a stellar mass ($M_\star = 0.584^{+0.025}_{-0.019} M_\odot$), compatible with the stellar mass derived from the period spacing, and in line with the spectroscopic mass ($M_\star = 0.560 \pm 0.028 M_\odot$). In agreement with previous works, we found that the frequency splittings vary according to the radial order of the modes, suggesting differential rotation. Obtaining a seismological model made it possible to estimate the seismological distance ($d_{\text{seis}} = 42.85 \pm 0.73$ pc) of GD 358, which is in very good accordance with the precise astrometric distance measured by *Gaia* EDR3 ($\pi = 23.244 \pm 0.024$, $d_{\text{Gaia}} = 43.02 \pm 0.04$ pc).

Conclusions. The high-quality data measured with the TESS space telescope, used in combination with data taken from ground-based observatories, provides invaluable information for conducting asteroseismological studies of DBV stars, analogously to what happens with other types of pulsating white-dwarf stars. The currently operating TESS mission, together with the advent of other similar space missions and new stellar surveys, will give an unprecedented boost to white dwarf asteroseismology.

Key words. white dwarfs – stars: oscillations – stars: interiors – stars: evolution – asteroseismology – methods: data analysis

* NSF Astronomy and Astrophysics Postdoctoral Fellow.

1. Introduction

Pulsating white dwarfs (WD) and pre-WDs constitute a long-studied and reliably established class of compact variable stars, both from observational and theoretical grounds. Their brightness variations are multiperiodic, with periods between 100 s and 7000 s, and amplitudes up to 0.4 mag in typical optical light curves (Winget & Kepler 2008; Fontaine & Brassard 2008; Althaus et al. 2010; Córscico et al. 2019). The variability is associated with low-degree ($\ell \leq 2$), nonradial g (gravity)-mode pulsations excited by a physical mechanism related to the partial ionization of the dominant chemical species in the zone of driving, located in the external layers. In warm and cool pulsating WDs, the opacity bumps associated with these partial-ionization zones are responsible for the appearance of an outer convection zone, which also strongly contributes to g -mode pulsation instabilities (Brickhill 1991; Goldreich & Wu 1999; Wu & Goldreich 1999). The first pulsating WD was discovered in 1968 (Landolt 1968), and currently more than 300 objects are known. They are classified in various categories, including DAVs or ZZ Ceti stars (pulsating WDs with H atmospheres), DBV or V777 Her stars (pulsating WDs with helium atmospheres), and pulsating PG 1159 or GW Vir stars, among others (Winget & Kepler 2008; Fontaine & Brassard 2008; Althaus et al. 2010; Córscico et al. 2019).

Since the discovery of the first pulsating WDs, observations of these variable stars have been steadily increasing, thanks to single-site observations and also multisite campaigns such as those of the Whole Earth Telescope (WET; Nather et al. 1990). Subsequently, a dramatic growth in the number of known pulsators was made possible thanks to the identification of candidates from the spectral observations of the Sloan Digital Sky Survey (SDSS, York et al. 2000; Kleinman et al. 2013; Kepler et al. 2015, 2016, 2019), examples of which are the works of Mukadam et al. (2004a,b, 2006). Finally, in recent years, the area has received a strong boost driven by the uninterrupted observations from space made by the *Kepler* telescope, including both the main mission (Borucki et al. 2010) and K2 mode (Howell et al. 2014). Indeed, these efforts paved the way for the analysis of 32 ZZ Ceti stars and three DBV stars (Østensen et al. 2011; Greiss et al. 2014; Bell et al. 2015, 2017; Hermes et al. 2017a,b; Bell 2017; Duan et al. 2021), until the mission was terminated due to a lack of fuel in 2018. The successor to *Kepler* is the Transiting Exoplanet Survey Satellite (TESS, Ricker et al. 2015). This space mission has observed 200 000 brightest stars in 85% of the whole sky in 2019 and 2020 in the first part of the mission. TESS performs extensive time-series photometry that allows one to discover pulsating stars and, in particular, variable hot subdwarfs, WDs, and pre-WDs with $\text{mag} < 16$, with a short (120 s) cadence. In July 2020, it started to observe in 20 s cadence.

Relevant to this work are the DBV stars, which are pulsating He atmosphere WDs with effective temperatures in the range $22\,400 \lesssim T_{\text{eff}} \lesssim 32\,000$ K and they pulsate with g -mode periods between 120 and 1080 s (Winget & Kepler 2008; Córscico et al. 2019). The existence of the DBV class of pulsating WDs was anticipated through theoretical arguments (Winget et al. 1982b) before it was confirmed observationally shortly after (Winget et al. 1982a). Pulsations in DBVs are thought to be excited by a combination of the κ mechanism acting in the He partial ionization zone – thus setting the blue edge of the DBV instability strip (Winget et al. 1983b) – and the “convective driving” mech-

anism (Brickhill 1991; Dupret et al. 2008; Quirion et al. 2008; Van Grootel et al. 2017).

Due to the high-quality *Kepler* and K2 observations, three DBV stars, KIC 8626021 (Østensen et al. 2011), PG 0112+104 (Hermes et al. 2017b), and EPIC 228782059 (Duan et al. 2021), were intensively studied with space data. In particular, KIC 8626021 has been repeatedly modeled by several independent research groups (Bischoff-Kim & Østensen 2011; Córscico et al. 2012; Bischoff-Kim et al. 2014; Giannicchele et al. 2018; Charpinet et al. 2019), who have explored its internal structure with unprecedented precision. The first DBV pulsator observed extensively with TESS, the star EC 0158–160 or WD 0158–160 (TIC 257459955), was analyzed and modeled by Bell et al. (2019), who found nine independent frequencies appropriate for asteroseismology.

In this work, we present new TESS observations of the known DBV star GD 358. It has been scrutinized extensively from the ground for three decades. While some time-series photometry of GD 358 has been obtained from space (e.g., Castanheira et al. 2005), in this work we examine this archetypal DBV star using intensive high-precision photometry from space for the first time. We also perform a detailed asteroseismological analysis of this star on the basis of the fully evolutionary models of DB WDs computed by Althaus et al. (2009). The present study is the third part of our series of papers devoted to the study of pulsating H-deficient WDs observed with TESS. The first article is focused on six known GW Vir stars (Córscico et al. 2021), and the second one is devoted to the discovery of two new GW Vir stars, specifically DOVs (Uzundag et al. 2021).

The paper is organized as follows. In Sect. 2 we provide a brief account of the main characteristics of GD 358. In Sect. 3, we describe the methods we applied to obtain the pulsation periods of the target star. A brief summary of the stellar models of DB WD stars employed for the asteroseismological analysis of GD 358 is provided in Sect. 4. Section 5 is devoted to the asteroseismological modeling of the target star, including the search for a possible uniform period spacing in the period spectrum by applying significance tests, the derivation of the stellar mass using the period separation, and the execution of a period-to-period fit with the goal of finding an asteroseismological model. Finally, in Sect. 6, we summarize our results.

2. The target star: GD 358

The location of GD 358 in the $T_{\text{eff}}-\log g$ diagram is depicted in Fig. 1. We have included the evolutionary tracks of DB WDs computed by Althaus et al. (2009). Independently of the precise location of GD 358 dictated by the spectroscopic parameters (see below), the star appears to be in the middle of the DBV instability strip, with a stellar mass somewhat lower than the average mass of the C/O-core WDs ($\sim 0.6 M_{\odot}$). We describe the basic characteristics of GD 358 below and summarize its stellar properties in Table 1. GD 358 (or V777 Her) has a TESS Input Catalog (TIC) number of TIC 219074038. It is the brightest ($m_V = 13.7$) and most extensively studied DBV star. This prototypical object provides the designation for the class of V777 Her (or DBV) variable stars. The pulsations of GD 358 were discovered in 1982 (Winget et al. 1982b). Its spectroscopic surface parameters are $T_{\text{eff}} = 24\,937 \pm 1018$ K and $\log g = 7.92 \pm 0.05$ according to Bédard et al. (2017) from optical data (see Fig. 1), although the previous analysis by Nitta et al. (2012) and Koester et al. (2014) using optical and UV data give $T_{\text{eff}} = 24\,000 \pm 500$ K and $\log g = 7.8 \pm 0.05$ (Fig. 1). Recently, Kong & Luo (2021) derived the atmospheric parameters of GD 358 with LAMOST data and

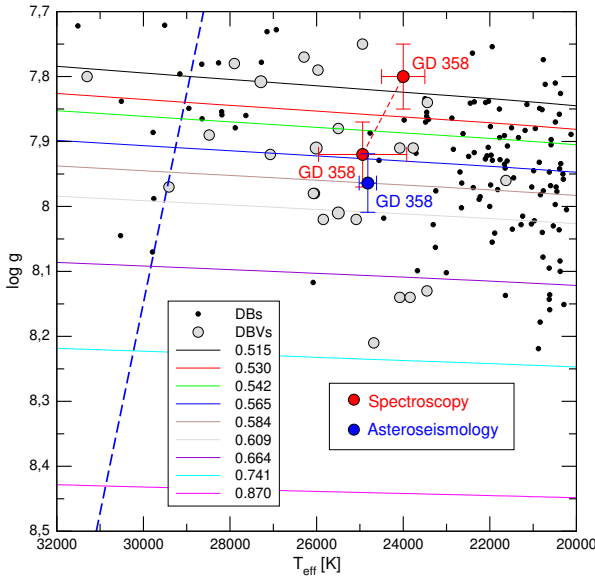


Fig. 1. Location of DB WDs on the T_{eff} – $\log g$ diagram (Kepler et al. 2019), marked with small black circles. Also depicted is the location of the published DBV stars (gray circles), according to the compilation by Córscico et al. (2019). The target star of the present paper, GD 358, is highlighted with large red circles according to spectroscopy; the two locations of this star correspond to two spectroscopic determinations of T_{eff} and $\log g$ according to Koester et al. (2014) ($T_{\text{eff}} = 24\,000 \pm 500$ K, $\log g = 7.80 \pm 0.05$), which are very close to the recent derivations by Kong & Luo (2021), and according to Bédard et al. (2017) ($T_{\text{eff}} = 24\,937 \pm 1018$ K, $\log g = 7.92 \pm 0.05$). The location of the asteroseismological model (see Sect. 5.2) is emphasized with a blue circle. The DB WD evolutionary tracks of Althaus et al. (2009) are displayed with different colors according to the stellar-mass values (in solar units). The blue-dashed line represents the theoretical dipole ($\ell = 1$) blue edge of the DBV instability strip, according to Córscico et al. (2009).

found $T_{\text{eff}} = 24\,075 \pm 124$ K and $\log g = 7.827 \pm 0.01$ dex. These values are in perfect agreement with the parameters derived by Nitta et al. (2012) and Koester et al. (2014). The spectroscopic parameters are summarized in Table 1. GD 358 has been extensively observed by the WET collaboration (Winget et al. 1994; Vuille et al. 2000; Kepler et al. 2003; Provencal et al. 2009). The most recent and complete analysis of this star was carried out by Bischoff-Kim et al. (2019), who collected and reduced data from 34 years of photometric observations, including archival data from 1982 to 2006, and 1195.2 h of observations from 2007 to 2016. Bischoff-Kim et al. (2019) detected a total of 15 independent periods, of which 13 belong to a series of $\ell = 1$ pulsation periods with consecutive radial order, which is the longest continuous sequence of periods observed in a DBV star until now. The star has repeatedly been the focus of asteroseismological analyses (Bradley & Winget 1994; Metcalfe et al. 2000, 2001; Fontaine & Brassard 2002; Metcalfe 2003) using evolutionary models of DB WDs with simplified chemical profiles. Bischoff-Kim et al. (2019) analyzed this star using models that include parameterized, complex, core-composition profiles to fit the 15 observed periods. They obtain a seismological model with a thickness of the He layer that is qualitatively consistent with the diffusion-calculation picture that predicts that the pure-He envelope will steadily grow thicker as the DB star cools (Dehner & Kawaler 1995; Fontaine & Brassard 2002;

Althaus & Córscico 2004). The *Gaia* EDR3 parallax and distance for GD 358 are $\pi = 23.244 \pm 0.024$ mas and $d = 43.02 \pm 0.04$ pc (Bailer-Jones et al. 2021), respectively.

3. Observations and data reduction

GD 358 was observed by TESS at a 2-min cadence on Sector 25 between 2020 May 13 and 2020 June 08, targeted as TIC 219074038 ($T = 13.9$ mag). The temporal resolution is $1/T = 0.451$ µHz (T being the data span of 25.67 days). The light curve for GD 358 released by the Science Processing Operations Center (SPOC) pipeline had large gaps, which we believe were caused by unnecessarily harsh clipping based on quality flags that resulted in a low (67.4%) duty cycle. We re-reduced the Sector 25 data with the same 5-pixel aperture from the SPOC pipeline, but with looser quality-flag cuts, yielding a significantly higher (92.6%) duty cycle. Our final light curve was flattened of long-term trends by the division of a second-order polynomial every 2 days. The final light curve is shown in Fig. 2, including 16781 data points spanning 25 days. The average noise level of the amplitude spectra is 0.24 ppt. We calculated a detection threshold of 0.1% false alarm probability (FAP) following the method described in Kepler (1993) (see also Baran & Koen 2021). If the amplitude of a given peak is above this value, there is a 0.1% chance it results from random noise fluctuations. All frequencies above the threshold level of 0.1% FAP of 1.45 ppt have been prewhitened with a few exceptions. The frequencies at 1657 and 2157 µHz are below the significance threshold with a signal-to-noise ratio (S/N) of 5.6 and 4.6 respectively. These frequencies were reported in the previous work by Bischoff-Kim et al. (2019). Moreover, we prewhitened eight combination frequencies, which are located beyond 2300 µHz. A few of them at 2315, 2530, 2912, and 3386 µHz are slightly below the 0.1% FAP level with an S/N of 5.3, 5.5, 4.7, and 5, respectively. All combination frequencies beyond 2400 µHz were detected for the first time and also extracted from the light curve and reported in Table 2. Overall, we detected 26 frequencies that are concentrated between 900 µHz and 3400 µHz, out of which we identified eight combination frequencies. Figure 2 displays the Fourier transform of GD 358. In Table 2, we show the list of periods of GD 358 detected with TESS.

The frequencies emphasized with boldface in Table 2 are components of rotational triplets ($\ell = 1$). Rotational multiplets are depicted in Fig. 3. A well-known property of nonradial stellar pulsations is that the eigenfrequencies of degree ℓ split into $2\ell + 1$ components differing in azimuthal (m) number due to stellar rotation. When the rotation is slow and rigid, the frequency splitting can be obtained as $\delta\nu_{\ell,k,m} = m(1 - C_{\ell,k})\Omega_R$, Ω_R being the rotational angular frequency of the pulsating star, and $m = 0, \pm 1, \pm 2, \dots, \pm \ell$ (Unno et al. 1989). The condition of slow rotation implies that $\Omega_R \ll \nu_{\ell,k}$. The $C_{\ell,k}$ constants are the Ledoux coefficients (Ledoux & Walraven 1958), which can be assessed as $C_{\ell,k} \sim [\ell(\ell + 1)]^{-1}$ in the asymptotic limit of high radial-order g modes ($k \gg \ell$). In the specific case of dipole ($\ell = 1$) and quadrupole ($\ell = 2$) modes, we have $C_{1,k} \sim 0.5$ and $C_{2,k} \sim 0.17$, respectively. In addition to allowing an estimate of the rotation speed of the star, multiplets in the frequency spectrum of a pulsating WD are very useful to identify the harmonic degree of the pulsation modes. This approach to derive the rotation period has been successfully applied to several pulsating WD stars (see, for instance, Hermes et al. 2017a, for the case of ZZ Ceti stars observed during the Kepler and K2 missions). Winget et al. (1994) detected ten complete (that is, with all three components) rotational triplets of frequencies in GD 358 as a

Table 1. Characteristics of GD 358.

TIC	Name	T_{eff} [K]	$\log g$ [cgs]	π [mas]	d [pc]
219074038	GD 358 (V777 Her)	24 937 ± 1018	7.92 ± 0.05	23.244 ± 0.024	43.02 ± 0.04
		24 000 ± 500	7.80 ± 0.05		
		24 075 ± 124	7.827 ± 0.01		
LAMOST J164718.35+322832.9					

Notes. Columns 1, 2, 3, 4, 5, and 6 correspond to the TESS input catalog number, name of the object, effective temperature, surface gravity, *Gaia* EDR3 parallax, and distance, respectively. There are three spectroscopic determinations of the atmospheric parameters, the first row corresponding to the values from Bédard et al. (2017), the second one from Nitta et al. (2012), Koester et al. (2014), and the third one from Kong & Luo (2021). For details, see the text.

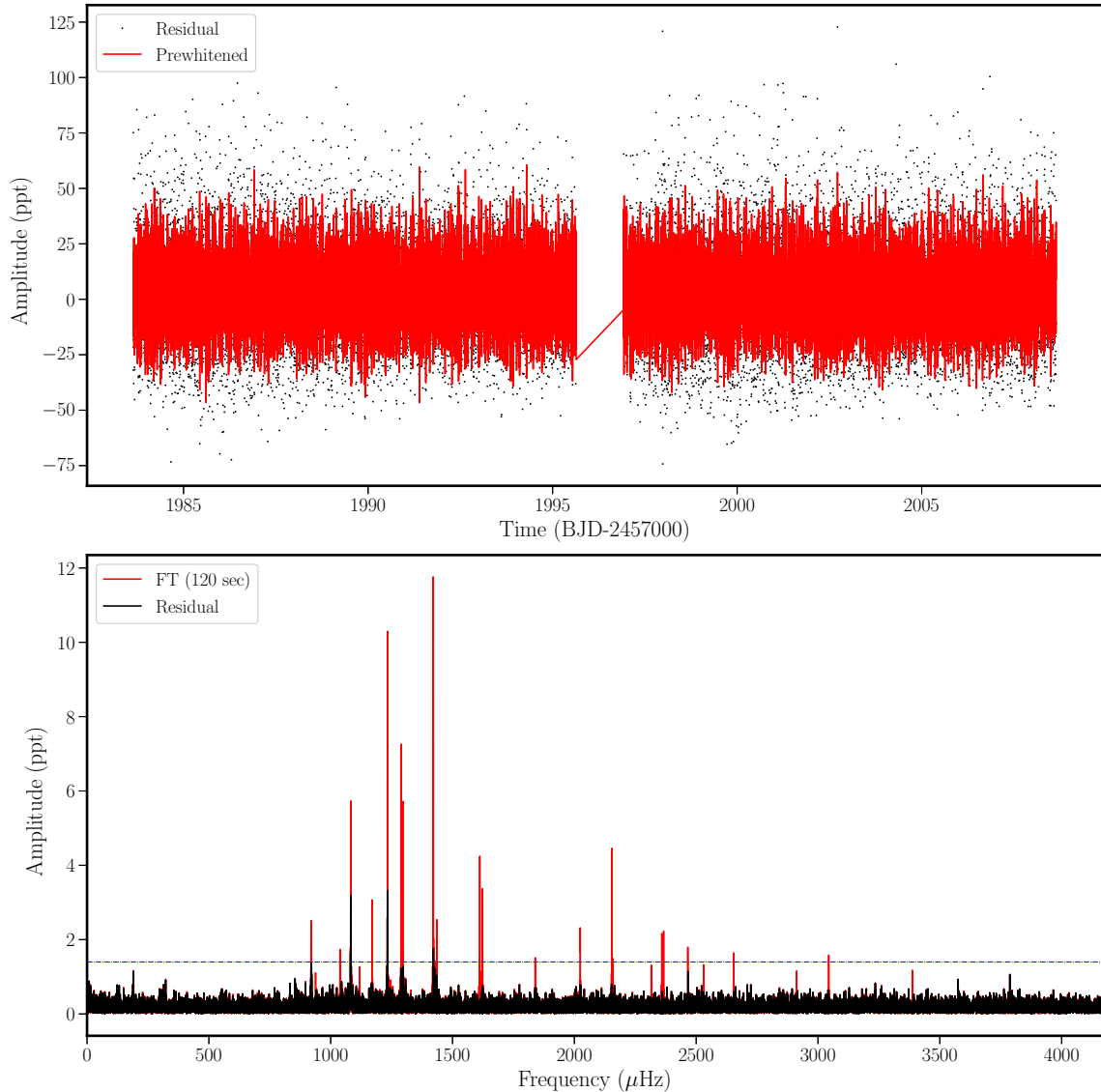


Fig. 2. *Top:* light curve of the pulsating DBV star GD 358 observed in sector 25. The black dots show the residual flux, while the red lines show all prewhitened variations from the light curve. *Bottom:* fourier transform of the pulsating DBV star GD 358 observed with 120-sec cadence. The dotted horizontal blue line indicates the 0.1% false-alarm-probability (FAP) significance threshold. The black line is the FT of the prewhitened light curve.

result of the intensive scrutiny of this star with the WET collaboration. These authors found that the frequency splittings ($\delta\nu$) are not constant, but vary with the radial order, which led them to conclude that the star could be experiencing differential rotation, with the outer envelope rotating twice as fast as the core (but see also Kawaler et al. 1999). Kepler et al. (2003) reported the absence of triplets in the 2000 data of GD 358, except for one clear triplet centered at $\sim 2154 \mu\text{Hz}$. Later, Provencal et al. (2009) found only two clear rotational triplets, centered at $\sim 2154 \mu\text{Hz}$ and $\sim 2363 \mu\text{Hz}$, and their analysis from 1990 to 2008 revealed a long-term change in the multiplet splittings coinciding with the 1996 *sforzando* event, where the star dramatically altered its pulsation characteristics on a timescale of hours. These phenomena could be attributed to the interaction between convection and/or magnetic fields and pulsations.

The TESS data of GD 358 presented in this work reveal the presence of four out of the ten triplets found in Winget et al. (1994). At variance with the results of that paper, in the TESS data, we found two complete triplets and two incomplete triplets. One of the complete triplets has frequencies of $2359.010 \mu\text{Hz}$, $2362.689 \mu\text{Hz}$, and $2366.318 \mu\text{Hz}$. Going to smaller frequencies, we found the other complete triplet with frequencies of $1623.248 \mu\text{Hz}$, $1617.409 \mu\text{Hz}$, and $1611.949 \mu\text{Hz}$, an incomplete triplet with frequencies of $1435.142 \mu\text{Hz}$ and $1421.059 \mu\text{Hz}$ ¹, and other incomplete triplet with frequencies of $1297.338 \mu\text{Hz}$ and $1289.082 \mu\text{Hz}$. These rotational triplets are emphasized in boldface in Table 2. We show the rotational triplets in Fig. 3. Similar to the findings of Winget et al. (1994), we found that the frequency splittings $\delta\nu$ in these four triplets are not constant, as we show in Sect. 5.1.

4. Evolutionary models, numerical codes, and spectroscopic masses

We employed a set of fully evolutionary DB WD stellar models that consider the whole evolution of the progenitor stars. Specifically, the stellar models were taken from the evolutionary calculations presented by Althaus et al. (2009) produced with the LPCODE evolutionary code. For details about the input physics and evolutionary code, and the numerical simulations performed to obtain the DB WD evolutionary sequences employed here, we refer the interested reader to that paper. These evolutionary tracks were employed in the asteroseismic analyses of the DBV stars KIC 8626021 (C  rsico et al. 2012), KUV 05134+2605 (Bogn  r et al. 2014), PG 1351+489 (C  rsico et al. 2014), and WD 0158–160 (Bell et al. 2019). The sequences of DB WD models were computed considering a detailed treatment of the prior evolution, starting from the zero-age main sequence (ZAMS), taking into account the thermally pulsing asymptotic giant branch (TP-AGB) and born-again (VLTP; very late thermal pulse) phases, the stage of the PG 1159 stars, and finally the DB WD phase. By virtue of this, the models have evolving chemical profiles consistent with the prior evolution. The models assume the ML2 prescription of

¹ Between these two frequencies, there is a frequency of $1426.986 \mu\text{Hz}$, but with a very low amplitude (1.294 ppt), which could be the $m = 0$ component of the triplet, although the splittings of the triplet would be quite different ($\delta\nu \sim 8 \mu\text{Hz}$ and $\delta\nu \sim 6 \mu\text{Hz}$). A peak of similar frequency ($1427.27 \mu\text{Hz}$) has been reported by Winget et al. (1994) with appreciable amplitude (19 ppt). However, we do not include the frequency of $1426.986 \mu\text{Hz}$ in this work since all periods detected in GD 358 from ground-based observations, such as those of Winget et al. (1994), are taken into account through the “mean periods” calculated by Bischoff-Kim et al. (2019); see Sect. 5.1.

Table 2. Identified frequencies (combination frequencies), periods, and amplitudes (and their uncertainties) and the signal-to-noise ratio in the data of GD 358.

Peak	ν (μHz)	Π (s)	A (ppt)	S/N
f₁	919.507 ± 0.018	1087.538 ± 0.021	2.521 ± 0.18	10.5
f₂	1038.177 ± 0.026	963.226 ± 0.025	1.739 ± 0.18	7.2
f₃	1082.770 ± 0.008	923.556 ± 0.007	5.723 ± 0.18	23.8
f₄	1170.146 ± 0.015	854.593 ± 0.011	3.115 ± 0.18	12.9
f₅	1232.928 ± 0.004	811.076 ± 0.003	10.325 ± 0.18	43.0
f₆	1289.082 ± 0.006	775.745 ± 0.003	7.212 ± 0.18	30.0
F3 f₇	1297.338 ± 0.008	770.808 ± 0.005	5.574 ± 0.18	23.2
F1 f₈	1421.059 ± 0.004	703.700 ± 0.002	11.782 ± 0.18	49.0
f₉	1435.142 ± 0.018	696.794 ± 0.009	2.530 ± 0.18	10.5
f₁₀	1611.949 ± 0.010	620.367 ± 0.004	4.327 ± 0.18	18.0
f₁₁	1617.409 ± 0.034	618.272 ± 0.013	1.352 ± 0.18	5.6
f₁₂	1623.248 ± 0.013	616.048 ± 0.005	3.403 ± 0.18	14.1
f₁₃	2024.182 ± 0.020	494.026 ± 0.005	2.280 ± 0.18	9.5
f₁₄	2154.064 ± 0.010	464.238 ± 0.002	4.360 ± 0.18	18.1
f₁₅	2157.584 ± 0.042	463.481 ± 0.009	1.109 ± 0.18	4.6
f₁₆	2359.010 ± 0.021	423.906 ± 0.003	2.214 ± 0.18	9.2
f₁₇	2362.689 ± 0.021	423.246 ± 0.003	2.169 ± 0.18	9.0
f₁₈	2366.318 ± 0.019	422.597 ± 0.003	2.380 ± 0.18	9.9
2f₁	1839.301 ± 0.031	543.684 ± 0.009	1.498 ± 0.18	6.2
f₃+f₅	2315.669 ± 0.036	431.840 ± 0.006	1.282 ± 0.18	5.3
2f₅	2465.756 ± 0.026	405.555 ± 0.004	1.772 ± 0.18	7.3
f₅+f₇	2530.302 ± 0.034	395.209 ± 0.005	1.337 ± 0.18	5.5
F2 f₅+f₈	2653.958 ± 0.028	376.795 ± 0.004	1.614 ± 0.18	6.7
F5 f₆+f₁₂	2912.290 ± 0.040	343.372 ± 0.004	1.147 ± 0.18	4.7
f₈+f₁₂	3044.295 ± 0.029	328.483 ± 0.003	1.586 ± 0.18	6.6
f₅+f₁₄	3386.984 ± 0.038	295.247 ± 0.003	1.213 ± 0.18	5.0

convection with the mixing length parameter, α , fixed to one (Bohm & Cassinelli 1971; Tassoul et al. 1990). Specifically, we considered nine DB WD sequences with stellar masses as follows: $0.515, 0.530, 0.542, 0.565, 0.584, 0.609, 0.664, 0.741$, and $0.870 M_{\odot}$. These DB WD sequences are characterized by the maximum He-rich envelope that can be left by prior evolution if we assume that they are the result of a born-again episode. The value of envelope mass ranges from $M_{\text{He}}/M_{\star} \sim 2 \times 10^{-2}$ ($M_{\star} = 0.515 M_{\odot}$) to $M_{\text{He}}/M_{\star} \sim 1 \times 10^{-3}$ ($M_{\star} = 0.870 M_{\odot}$). In Fig. 1, we show the complete set of DB WD evolutionary tracks (with different colors according to the value of the stellar mass) along with the location of all the DBVs known to date (C  rsico et al. 2019), including GD 358. The $\ell = 1, 2$ g-mode pulsation periods employed in this work were computed with the adiabatic and nonadiabatic versions of the pulsation code LP-PUL (C  rsico & Althaus 2006; C  rsico et al. 2006, 2009) and the same methods employed in the previous works of de La Plata Stellar Evolution and Pulsation Research Group².

We assessed a value of the spectroscopic mass of GD 358 by interpolation on the evolutionary tracks presented in Fig. 1 and the published values of the spectroscopic surface gravity and temperature. This is a relevant aspect because this same set of DB WD models was employed to derive the stellar mass from the period spacing (next section). We get an spectroscopic stellar mass of $M_{\star} = 0.508 \pm 0.050 M_{\odot}$ if $T_{\text{eff}} = 24\,000 \pm 500 \text{ K}$ and $\log g = 7.80 \pm 0.05$ (Nitta et al. 2012), and $M_{\star} = 0.560 \pm 0.028 M_{\odot}$ if $T_{\text{eff}} = 24\,937 \pm 1018 \text{ K}$ and $\log g = 7.92 \pm 0.05$ (B  dard et al. 2017). The uncertainties in the stellar mass were

² <http://fcaglp.fcaglp.unlp.edu.ar/evolgroup/>

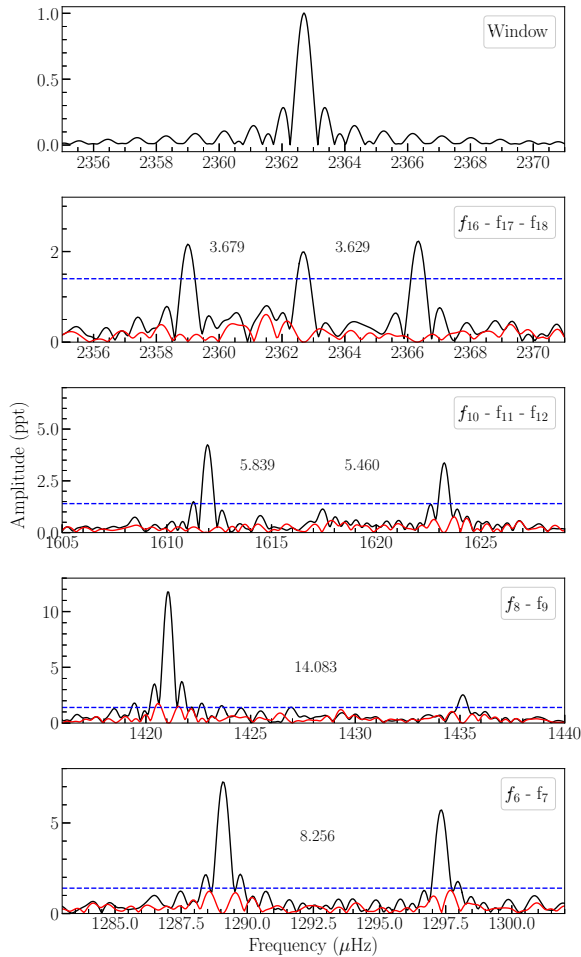


Fig. 3. Rotational triplets in the frequency spectrum of GD 358. The FT are shown with black lines, and residuals with red lines. The blue-dashed horizontal lines correspond to 0.1% FAP confidence levels. The upper panel is the window function.

derived from the errors in T_{eff} and $\log g$ adopting the extreme values of these parameters when interpolating between the evolutionary tracks of Fig. 1.

5. Asteroseismology

In the asymptotic limit of high-radial orders ($k \gg \ell$), the periods of g modes with a consecutive radial order are approximately evenly separated (Tassoul et al. 1990), with the constant period spacing being dependent on the harmonic degree:

$$\Delta\Pi_{\ell}^{\text{a}} = \frac{\Pi_0}{\sqrt{\ell(\ell+1)}}, \quad (1)$$

with Π_0 being a constant value defined as follows:

$$\Pi_0 = \frac{2\pi^2}{\left[\int_{r_1}^{r_2} \frac{N}{r} dr \right]}, \quad (2)$$

where N is the Brunt-Väisälä frequency. The asymptotic period spacing given by Eq. (1) is very close to the computed period

spacing of g modes in chemically homogeneous stellar models without convective regions (Tassoul 1980). In the case of pulsating DB WDs, they may have a surface convective zone, although it is usually very thin compared to the stellar radius. On the other hand, they have several chemical composition gradients. Mainly for this last reason, the calculated period spacing does not coincide with the asymptotic period spacing given by Eq. (1); nevertheless, the average of the calculated spacing is very close to $\Delta\Pi_{\ell}^{\text{a}}$ for radial orders that are high enough. The departures of the period spacing from the averaged period spacing are provoked by the mechanical resonance called “mode trapping”. Mode trapping has been intensively studied in the context of DAV, DBV, and GW Vir stars (see, e.g., Brassard et al. 1992; Bradley et al. 1993; Kawaler & Bradley 1994; Córscico et al. 2002; Córscico & Althaus 2006).

The methods used in this paper to extract information pertaining to the stellar mass and the internal structure of GD 358 are the same as those employed in Córscico et al. (2021) for GW Vir stars observed with TESS (see, also, Córscico et al. 2012, 2014; Bognár et al. 2014; Bell et al. 2019). Specifically, we compared the observed period spacing of GD 358 ($\Delta\Pi$) with the asymptotic period spacing ($\Delta\Pi_{\ell}^{\text{a}}$) computed with Eq. (1) at the effective temperature of the star to derive an estimate of the stellar mass. DBV stars generally do not have all of their pulsation modes in the asymptotic regime, so there is usually no perfect agreement between $\Delta\Pi$ and $\Delta\Pi_{\ell}^{\text{a}}$. Therefore, the derivation of the stellar mass using the asymptotic period spacing may not be entirely reliable in DBV stars that pulsate with modes characterized by low and intermediate radial orders, but it gives a good estimate of the stellar mass for stars pulsating with g modes of a high radial order (see Althaus et al. 2008, for the case of GW Vir stars). A variation of this approach to infer the stellar mass of DBV stars is to compare $\Delta\Pi$ with the average of the computed period spacings ($\overline{\Delta\Pi_k}$). It is calculated as $\overline{\Delta\Pi_k} = (n-1)^{-1} \sum_k \Delta\Pi_k$, where the “forward” period spacing ($\Delta\Pi_k$) is defined as $\Delta\Pi_k = \Pi_{k+1} - \Pi_k$ (with k being the radial order) and n is the number of computed periods laying in the range of the observed periods. This method is more reliable for the estimation of the stellar mass of DBV stars than that described above using $\Delta\Pi_{\ell}^{\text{a}}$ because, provided that the average of the computed period spacings is evaluated at the appropriate range of periods, the approach is valid for the regimes of short, intermediate, and long periods as well. When the average of the computed period spacings is taken over by a range of periods characterized by high k values, then the predictions of the present method become closer to those of the asymptotic period-spacing approach (Althaus et al. 2008). On the other hand, the present method requires detailed period computations, as opposed to the method described above, which does not involve pulsational calculations. We note that both methods for assessing the stellar mass rely on the spectroscopic effective temperature, and the results are unavoidably affected by its associated uncertainty. The methods outlined above take full advantage of the fact that the period spacing of DBV stars primarily depends on the stellar mass and the effective temperature, and very weakly on the thickness of the He envelope (see, e.g., Tassoul et al. 1990)³.

A powerful approach to study the internal structure of pulsating stars is to search for models that best fit the observed

³ These methods cannot, in principle, be directly applied to DAV stars to infer the stellar mass, for which the period spacing depends, simultaneously, on M_{\star} , T_{eff} , and M_{H} with a comparable sensitivity, and this implies the existence of multiple combinations of these three quantities that produce the same spacing of periods.

pulsation periods. To quantify the goodness of the match between the theoretical periods ($\Pi_{\ell,k}$) and the observed periods (Π_i^o), we followed the same procedure as in our previous studies:

$$\chi^2(M_\star, T_{\text{eff}}) = \frac{1}{N} \sum_{i=1}^N \min[(\Pi_{\ell,k} - \Pi_i^o)^2], \quad (3)$$

with N being the number of observed periods. In order to find the stellar model that best fits the observed periods exhibited by GD 358 –the “asteroseismological” model– we evaluated the function χ^2 for stellar masses $M_\star = 0.515, 0.530, 0.542, 0.565, 0.584, 0.609, 0.664, 0.741, 0.870 M_\odot$. For the effective temperature, we employed a very fine model grid ($\Delta T_{\text{eff}} = 10\text{--}30\text{ K}$). The DB WD model that shows the smallest value of χ^2 was adopted as the best-fit asteroseismological model. Below, we employ the tools described above to extract information pertaining to GD 358.

5.1. Period spacing and the seismic mass

Ground-based photometric observations of GD 358 span a period of 34 years. No other DBV star has been studied for such a long period of time, which is why we know the most about this object. A detailed compilation of the observations, including archival data from 1982 to 2006 and 1195.2 h of new observations from 2007 to 2016, has been presented by Bischoff-Kim et al. (2019). Figure 4 of that paper, which was constructed on the basis of the periods and amplitudes of their Tables 2 and 3, is extremely illustrative of how the periods of pulsation in this star are concentrated in bands with finite widths, rather than discrete periods. Frequencies detected in a given observing season are not found in all observing runs, and most of the detected frequencies are not statistically identical from year to year. Only a few frequencies appear with exactly the same values at various observing runs. Regarding the bands of periods exhibited by GD 358, Bischoff-Kim et al. (2019) find a general increase in their width with decreasing frequency (increasing period), at least until the band at 1238 μHz (807 s). This behavior could be related to the oscillation of the outer convection zone of the WD during pulsations (Montgomery et al. 2020). Specifically, the oscillation in the base of the convection zone would affect the radial eigenfunction of g modes that have the outer turning point of oscillation located precisely at the base of the outer convection zone. We note, however, that if the reason for the existence of bands of periods in GD 358 is the oscillation of the base of the outer convective zone, then the overall structure of the star remains largely unchanged.

While the origin of this phenomenon is not entirely clear and deserves further exploration, we note that the existence of finite bands of periods poses a problem for applying the asteroseismological tools, because they require a set of discrete observed periods (even with possible uncertainties) that must be compared with well-defined periods calculated in stellar models of WDs. To tackle this difficulty, Bischoff-Kim et al. (2019) determined the mean periods for each band to be used in the asteroseismic fits (see their Table 5). The use of the mean values of periods in asteroseismology is well-justified given that the periods do not change secularly, but they remain within a limited range of periods forming each band. In the lower and middle panels of Fig. 4, we show schematically all the periods detected from ground-based observations and the mean periods determined by Bischoff-Kim et al. (2019) for each band, respectively. The amplitude was arbitrarily set to one to facilitate

visualization. The period at 1014.35 s in the middle panel, represented with a red-dashed line, is not associated with any specific band, but instead corresponds to a single detection in the 2016 ground-based observations. In the upper panel of Fig. 4, we include the 18 periods detected by TESS (Table 2). By comparing the mean periods (middle panel) and the periods detected by TESS (upper panel), we note that there are at least nine periods that coincide between both sets at ~ 420 s, ~ 465 s, ~ 495 s, ~ 620 s, ~ 700 s, ~ 770 s, ~ 810 s, ~ 855 s, and ~ 970 s. Other periodicities are present in the ground-based mean periods, but not in the TESS periods (~ 540 s, ~ 575 s, ~ 660 s, ~ 730 s, ~ 902 s, ~ 1015 s, and ~ 1063 s), and vice versa (~ 925 s and ~ 1090 s). The space-based detection of nine periods already found from ground-based observations is a great finding in itself, because it confirms the results derived from exhaustive previous studies. Likewise, the detection of two additional signals which were not detected in previous works, allows us to broaden the spectrum of periods available for the asteroseismological study of this star. In fact, in order to extract as much information as possible with the tools of asteroseismology, it is crucial to employ as many periods (which represent eigenvalues of the star) as possible. In order to identify the pulsation modes and determine the possible period spacing of GD 358, which is essential to estimating the stellar mass, we considered an expanded list of periods by combining the 15 dipole $m = 0$ mean periods found by Bischoff-Kim et al. (2019) to the set of periods measured by TESS (Table 2). In the case of the nine periods close to one another detected in both data sets, we decided to adopt the periods measured by TESS because they are more accurate in general. In the case of the periods near 700 s, we adopted the period 699.82 s from Bischoff-Kim et al. (2019), which seems to be the central component of the incomplete rotational triplet $(+1, 0, -1) = (696.794 \text{ s}, \dots, 703.700 \text{ s})$ detected by TESS (see below). The resulting extended list of periods to be used in our analysis contains 26 periods and is shown in the first and second columns of Table 3. We note that we also considered the period 1014.35 s, which has only been detected in the observations of 2016. This period was not considered in the asteroseismological analysis of Bischoff-Kim et al. (2019). However, since its value seems to fit in the apparent pattern of dipole periods very well with a constant separation present in this star, as can be guessed from Fig. 4, we decided to include it in our subsequent analysis. We consider a proper procedure to combine periods detected at different times and both with observations from the ground and from space. We have the excellent example of the DAV star G29–38 (Kleinman et al. 1998), where a global pulsation spectrum for this star was constructed using different ground-based observations from a decade. Whatever the physical mechanism behind the alternate appearance and disappearance of modes, we can perform robust asteroseismological analyses by collecting the data from all epochs and constructing a combined spectrum of pulsations. This has been demonstrated for the DBV star KIC 08626021 (see Bischoff-Kim & Østensen 2011; Bischoff-Kim et al. 2014; Giambicche et al. 2018).

In the case of the rotational triplets, we assigned the m value to the different components following Winget et al. (1994). We note that the frequency splittings are not constant among the different triplets. In fact, we have $\delta\nu = 3.679 \mu\text{Hz}$ and $\delta\nu = 3.629 \mu\text{Hz}$ for the complete triplet centered at 2362.689 μHz (423.246 s), $\delta\nu = 5.839 \mu\text{Hz}$ and $\delta\nu = 5.460 \mu\text{Hz}$ for the complete triplet centered at 1617.409 μHz (618.272 s), 2 $\delta\nu = 14.083 \mu\text{Hz}$ (that is, $\delta\nu = 7.042 \mu\text{Hz}$) for the incomplete triplet with side components of 1435.142 μHz (696.794 s) and 1421.059 μHz (703.700 s), and $\delta\nu = 8.256 \mu\text{Hz}$ for the incomplete triplet centered at 1289.082 μHz (775.745 s). There is an

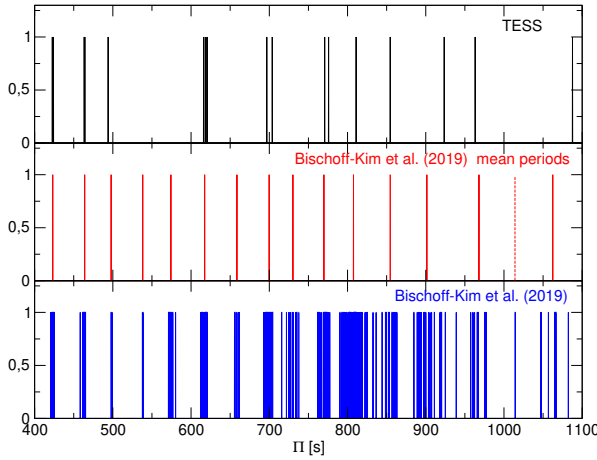


Fig. 4. Illustrative distribution of the periods of GD 358 according to TESS (19 periods, black lines, upper panel), and according to Bischoff-Kim et al. (2019) (15 mean periods, red lines, middle panel, and 352 periods, blue lines, lower panel). The period at 1014.35 s in the middle panel, represented with a red-dashed line, corresponds to a single detection in the 2016 ground-based observations. The amplitudes have been arbitrarily set to one for clarity.

apparent trend of larger $\delta\nu$ for decreasing frequencies (increasing periods), in agreement with Winget et al. (1994) (see their Fig. 6 and Table 2). This dependence of the frequency splittings with the radial order of the modes could indicate differential rotation of GD 358, since each mode samples areas of a different depth in the star, and this would indicate different speeds of rotation⁴. While these results would imply that GD 358 does not rotate as a rigid body, in order to confirm this, it would be necessary to make a detailed analysis such as that carried out by Kawaler et al. (1999) (see, also, Corsico et al. 2011, for the specific case of the GW Vir star PG 122+200), which is beyond the scope of this paper.

We looked for a constant period spacing in the data of GD 358 using the Kolmogorov-Smirnov (K-S; Kawaler 1988), and the inverse variance (I-V; O'Donoghue 1994) statistical tests. Figure 5 displays the results of applying the K-S and I-V significance tests to the period spectrum of GD 358. We show the case in which we adopted the full set of 352 periods of Tables 2 and 3 of Bischoff-Kim et al. (2019) (blue curves), and the situation in which the TESS periods plus the mean periods of Bischoff-Kim et al. (2019) (green curves) are considered. In this last case, we also considered the period at 1014.35 s which was disregarded in that paper. The two tests point to the existence of a pattern of $\ell = 1$ constant period spacing of $\Delta\Pi \sim 39$ s.

To derive a refined value of the period spacing, we carried out a linear least-squares fit to the 13 periods marked with an asterisk in Table 3 (see Fig. 6). These periods are all supposed to be the $\ell = 1 m = 0$ members of a sequence of periods equally spaced. We obtain a period spacing of $\Delta\Pi = 39.25 \pm 0.17$ s. This period spacing corresponds to our expectations for a dipole ($\ell = 1$) sequence. On the other hand, if we assume that the ~ 39 s period spacing were due to quadrupole modes, then the dipole

Table 3. Enlarged list of periods of GD 358.

Π_i^O (s) BK19	Π_i^O (s) TESS	Π_{fit} (s)	$\delta\Pi$ (s)	ℓ^O	m^O
	422.597			1	+1
	423.246*	421.697	1.549	1	0
	423.906			1	-1
	463.481*	460.942	2.539	1	0
	464.238			?	?
	494.026			?	?
538.30*	539.433	-1.133	1	0	
574.22*	578.678	-4.458	1	0	
	616.048			1	+1
	618.272*	617.923	0.349	1	0
	620.367			1	-1
658.69*	657.168	1.522	1	0	
	696.794			1	+1
699.82*	696.414	3.406	1	0	
	703.700			1	-1
730.28*	735.659	-5.379	1	0	
	770.808			1	+1
	775.745*	774.904	0.841	1	0
	811.076*	814.149	-3.073	1	0
	854.593*	853.394	1.199	1	0
901.49				?	?
	923.556			?	?
	963.226			?	?
1014.35*	1010.575	3.775	1	0	
1062.32				?	?
	1087.538*	1088.866	-1.328	1	0

Notes. Column 1 corresponds to seven $\ell = 1 m = 0$ average periods derived by Bischoff-Kim et al. (2019) (BK19). We also include the period at 1014.35 s extracted from the ground-based observations of 2016 (see Table 3 of Bischoff-Kim et al. 2019). Column 2 corresponds to 18 periods detected by TESS (Table 2). The periods with an asterisk are the 13 periods used in the linear least square fit depicted in Fig. 6.

period spacing would be ~ 68 s, which is not present in the tests⁵. Thus, the identification of the ~ 39 s period spacing as due to a sequence of dipole modes is robust. This sequence includes the 13 periods marked with an asterisk in Table 3, and the seven periods that are the $m = -1$ or $m = +1$ components of the four triplets. The remaining six periods in that table can be associated with $\ell = 1$ modes which, due to mode trapping effects, substantially deviate from the derived sequence of almost equally spaced periods, or with modes with $\ell = 2$ (or possibly higher) modes. In short, we have a total of 20 periods identified with $\ell = 1$ modes.

In the lower panel of Fig. 6, we show the residuals ($\delta\Pi$) between the dipole observed periods (Π_i^O) and the periods derived from the mean period spacing (Π_{fit}). The average of the absolute values of the residuals is $|\delta\Pi| = 2.35$ s. The existence of several minima in the distribution of residuals strongly suggests the mode-trapping effects inflicted by the presence of internal chemical transition regions.

We calculated the average of the computed period spacings for $\ell = 1$, $\overline{\Delta\Pi_k}$, in terms of the effective temperature for all the masses considered and a period interval of 400–1100 s, corresponding to the range of periods exhibited by GD 358. The results are shown in Fig. 7, where we depict $\overline{\Delta\Pi_k}$ with curves

⁴ We note that it makes no sense to calculate different rotational periods for GD 358 using the different frequency splittings using the uniform-rotation formula described in Sect. 3.

⁵ If such a dipole period spacing of ~ 68 s existed, it would involve an extremely low stellar mass for GD 358, which can safely be ruled out.

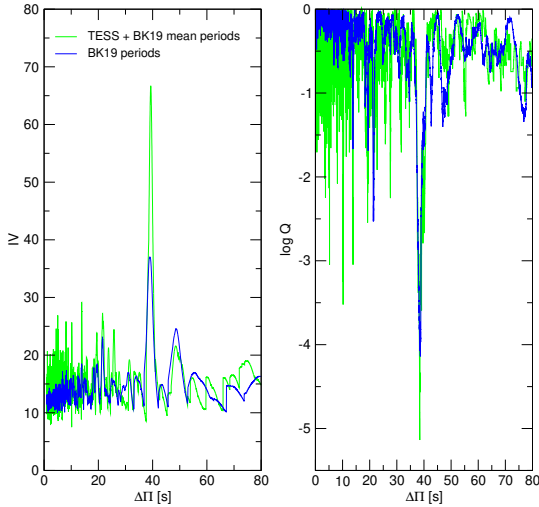


Fig. 5. I-V (left panel) and K-S (right panel) significance tests to search for a constant period spacing in GD 358. The tests were applied to the complete set of 352 pulsation periods of Tables 2 and 3 of Bischoff-Kim et al. (2019) (blue curves), and to the combination of the TESS periods plus the mean periods of Bischoff-Kim et al. (2019) (green curves), included in Table 3. A clear signal of a constant period spacing at ~ 39 s is evident. See text for details.

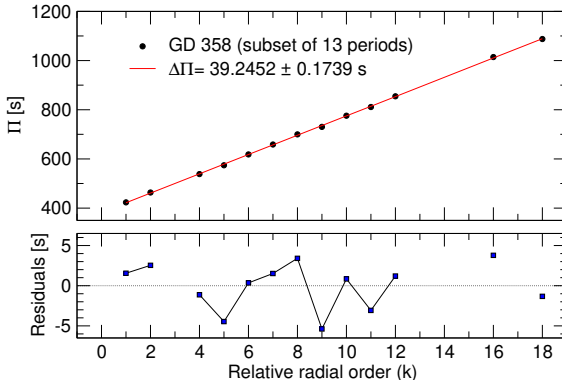


Fig. 6. Upper panel: linear least-squares fit to the 13 periods of GD 358 marked with asterisks in Table 3. The derived period spacing from this fit is $\Delta\Pi = 39.25 \pm 0.17$ s. Lower panel: residuals of the period distribution relative to the mean period spacing, revealing signals of mode trapping in the period spectrum of GD 358. Modes with a consecutive radial order are connected with thin black lines.

of different colors according to the various stellar masses. For the location of GD 358, indicated by a small red circle with error bars, we considered the average of the effective temperature, $T_{\text{eff}} = 24469 \pm 1018$ K, based on the effective temperatures derived by Bédard et al. (2017) and Koester et al. (2014). We performed a linear interpolation and obtain $M_{\star} = 0.588 \pm 0.024 M_{\odot}$.

5.2. Period fits and the asteroseismological model

In our analysis of period-to-period fits, we only took into account the components $m = 0$ present in the frequency spectrum of GD 358, and ignored the $m \neq 0$ components. In total, we have 19

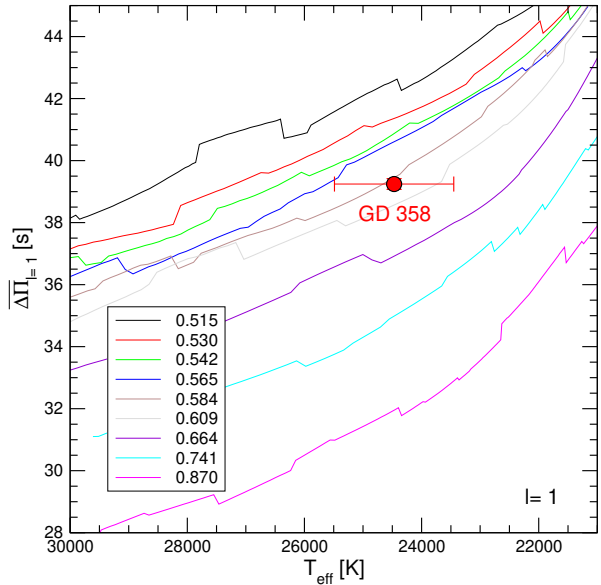


Fig. 7. Dipole ($\ell = 1$) average of the computed period spacings, $\overline{\Delta\Pi}_{\ell=1}$, evaluated in a range of periods that embraces the periods observed in GD 358, shown as curves of different colors for different stellar masses. We consider a mean effective temperature for the star, $T_{\text{eff}} = 24469 \pm 1018$ K, resulting from averaging $T_{\text{eff}} = 24000 \pm 500$ K (Koester et al. 2014) and $T_{\text{eff}} = 24937 \pm 1018$ K (Bédard et al. 2017). We adopted the mean period spacing $\Delta\Pi = 39.25 \pm 0.17$ s derived in Sect. 5.1. We include the error bars associated with the uncertainties in $\overline{\Delta\Pi}_k$ and T_{eff} . The stellar mass derived by interpolation is $M_{\star} = 0.588 \pm 0.024 M_{\odot}$.

observed periods as the input for our asteroseismological period fits (see Col. 1 of Table 4). According to the results derived in Sect. 5.1, we can assume that a subset of 13 $m = 0$ periods are associated with $\ell = 1$ modes – those marked with an asterisk in Table 3 – and we leave free the identification as $\ell = 1$ or $\ell = 2$ for the remaining six periods at the outset. We display our results in Fig. 8. We found three possible solutions, that is, maxima of $(\chi^2)^{-1}$, labelled as (1), (2), and (3), which are compatible with both effective temperature determinations of GD 358 and its uncertainties. These solutions are (1) $T_{\text{eff}} = 24967$ K and $M_{\star} = 0.584 M_{\odot}$ ($\chi^2 = 9.921$), (2) $T_{\text{eff}} = 25712$ K and $M_{\star} = 0.565 M_{\odot}$ ($\chi^2 = 11.758$), and (3) $T_{\text{eff}} = 24240$ K and $M_{\star} = 0.609 M_{\odot}$ ($\chi^2 = 17.595$). Clearly, the optimal solution is (1), since the DB WD model associated with it provides the best agreement between the theoretical and observed periods. We note that the effective temperature of this model is very close to that of GD 358 according to the spectroscopic determination of Bédard et al. (2017).

We adopted the model characterized by $M_{\star} = 0.584 M_{\odot}$, $T_{\text{eff}} = 24967$ K, and $\log(L_{\star}/L_{\odot}) = -1.215$ as the asteroseismological model for GD 358. The location of this model in the $\log g - T_{\text{eff}}$ diagram is displayed in Fig. 1 with a blue circle. In Table 4 we show a detailed comparison of the observed periods of GD 358 and the theoretical $m = 0$ periods of the asteroseismological model. According to this model, the periods exhibited by the star correspond to 16 dipole $m = 0$ modes with a radial order k in the range $k \in [8, 25]$, and three quadrupole modes with $36 \leq k \leq 43$. The average of the computed $\ell = 1$ period spacings for this model is $\overline{\Delta\Pi}_{\ell=1} = 38.926$ s, which is very similar to the dipole mean period spacing obtained in Sect. 5.1 for this

Table 4. Observed and theoretical $m = 0$ periods of the asteroseismological model for GD 358 [$M_\star = 0.584 M_\odot$, $T_{\text{eff}} = 24\,967 \text{ K}$, $\log(L_\star/L_\odot) = -1.215$] corresponding to solution (1) in Fig. 8.

Π_i^0 (s)	ℓ^0	Π_k (s)	ℓ	k	$\delta\Pi_k$ (s)	$\dot{\Pi}_k$ (10^{-13} s/s)	Unstable
423.246	1	420.975	1	8	2.272	0.725	Yes
463.481	1	462.511	1	9	0.970	1.354	Yes
464.238	?	462.511	1	9	1.727	1.354	Yes
494.026	?	499.054	1	10	-5.028	1.146	Yes
538.300	1	538.126	1	11	0.174	1.394	Yes
574.220	1	572.947	1	12	1.273	1.041	Yes
618.272	1	617.647	1	13	0.625	1.319	Yes
658.690	1	657.517	1	14	1.173	1.735	Yes
699.820	1	696.097	1	15	3.723	1.650	Yes
730.280	1	732.797	1	16	-2.517	1.506	Yes
775.745	1	770.251	1	17	5.494	1.621	Yes
811.076	1	812.662	1	18	-1.586	2.014	Yes
854.593	1	853.775	1	19	0.818	2.026	Yes
901.490	?	894.617	2	36	6.873	2.176	Yes
923.556	?	926.073	1	21	-2.517	1.900	Yes
963.226	?	965.149	2	39	-1.923	2.704	Yes
1014.350	1	1010.499	1	23	3.851	2.470	Yes
1062.320	?	1063.670	2	43	-1.350	3.004	Yes
1087.538	1	1082.719	1	25	4.819	2.420	Yes

Notes. We note that $\delta\Pi_k = \Pi_i^0 - \Pi_k$ represents the period differences, ℓ the harmonic degree, and k the radial order. The last column gives information about the pulsational stability and instability nature of the modes.

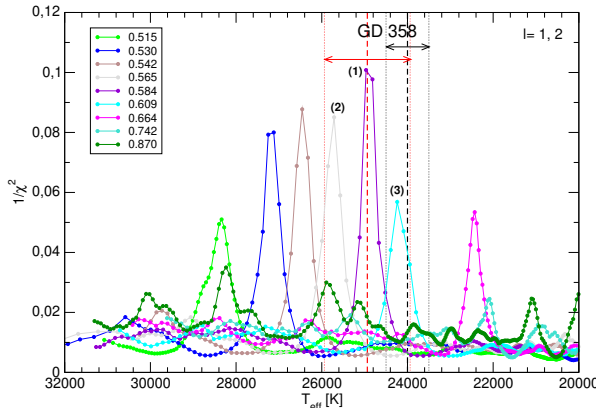


Fig. 8. Inverse of the quality function of the period fit in terms of the effective temperature, shown with different colors for the different stellar masses. The vertical black-dashed line corresponds to the spectroscopic T_{eff} of GD 358 and the vertical dotted lines show its uncertainties ($T_{\text{eff}} = 24\,000 \pm 500 \text{ K}$; Koester et al. 2014). Analogously, the blue vertical lines correspond to the spectroscopic T_{eff} and its uncertainties as given by Bédard et al. (2017) ($T_{\text{eff}} = 24\,937 \pm 1\,018 \text{ K}$). Three maxima have been labeled as (1), (2), and (3), corresponding to the three asteroseismological solutions compatible with spectroscopy (see the text).

star, $\Delta\Pi = 39.25 \pm 0.17 \text{ s}$. In order to quantitatively assess the goodness of our period-to-period fit, we computed the average of the absolute period differences, $\overline{\delta\Pi_i} = (\sum_{i=1}^n |\delta\Pi_i|)/n$, where $\delta\Pi_i = (\Pi_{\ell,k} - \Pi_i^0)$ and $n = 19$, and the root-mean-square residual, $\sigma = \sqrt{(\sum_{i=1}^n |\delta\Pi_i|^2)/n} = \sqrt{\chi^2}$. We obtain $\overline{\delta\Pi_i} = 2.56 \text{ s}$ and $\sigma = 3.15 \text{ s}$. To have a global indicator of the quality of the period fit that takes the number of free parameters, the number of fitted periods, and the proximity between the theoretical and observed

periods into account, we computed the Bayes information criterion (BIC; Koen & Laney 2000)⁶:

$$\text{BIC} = n_p \left(\frac{\log N}{N} \right) + \log \sigma^2, \quad (4)$$

with n_p being the number of free parameters of the models, and N the number of observed periods. The smaller the value of BIC, the better the quality of the fit. We note that this criterion introduces a penalty term for an excess in the number of parameters in the model. In our case, $n_p = 2$ (stellar mass and effective temperature), $N = 19$, and $\sigma = 3.15 \text{ s}$. We obtain $\text{BIC} = 1.13$ for the asteroseismological model, this value being the smallest among the possible solutions (1), (2), and (3) shown in Fig. 8. Also, the obtained BIC value is similar to that derived by Bischoff-Kim et al. (2019) ($\text{BIC} = 1.2$) for their best period fit to GD 358. The low value of BIC obtained in this work indicates that our period fit is very good.

Table 4 also includes the secular rates of period change ($\dot{\Pi} \equiv d\Pi/dt$) expected for each g mode of GD 358. We note that all of them are positive ($\dot{\Pi} > 0$), meaning that the periods are lengthening over time. The rate of change of periods in WDs and pre-WDs is related to \dot{T} (with T being the temperature at the region of the period formation) and R_\star (with R_\star being the stellar radius) through the approximate expression $(\dot{\Pi}/\Pi) \approx -a(\dot{T}/T) + b(R_\star/T)$ (Winget et al. 1983a). According to our asteroseismological model, the star is cooling with an approximately constant stellar radius. As a consequence, $\dot{T} < 0$ and $R_\star \sim 0$, and then, $\dot{\Pi} > 0$. We wonder if we could compare these theoretical estimates of the secular drift of the periods with the true rates of period change of GD 358. The frequencies (periods) $2362.689 \mu\text{Hz}$ (423.246 s) and $2154.064 \mu\text{Hz}$ (464.238 s) of GD 358, corresponding to the g modes with $k = 8$ and $k = 9$ according to our asteroseismological model, are the most stable frequencies of this star (Kepler et al. 2003; Provencal et al. 2009). However, the frequency shifts are large enough to mask any possible signs of evolutionary period change. Thus, we are forced to conclude that the observed periods of GD 358 are not stable enough to be able to measure the rate of change of periods due to the evolution of the star. This means that the values derived for the rate of change of periods of our seismological model of GD 358 remain (for now) only of academic interest.

We have also studied the pulsational stability and instability nature of the modes associated with the periods fitted to the observed ones. We assumed the frozen-in convection approximation (Unno et al. 1989). In particular, we examined the sign and magnitude of the linear nonadiabatic growth rates, $\eta_k = -\Im(\sigma_k)/\Re(\sigma_k)$, where $\Re(\sigma_k)$ and $\Im(\sigma_k)$ are the real and the imaginary parts of the complex eigenfrequency σ_k , respectively. A positive value of η_k means that the mode is linearly unstable (eighth column of Table 4). In the left (right) hand panel of Fig. 9, we show the instability domain of $\ell = 1$ ($\ell = 2$) periods as a function of the effective temperature for the DB WD model sequence with $M_\star = 0.584 M_\odot$. The palette of colors (right-hand scale) indicates the logarithm of the e -folding time, τ_e (in years) of each excited mode, being $\tau_e = 1/|\Im(\sigma_k)|$. Many pulsation modes are excited, and the interval of periods corresponding to unstable modes of our asteroseismological model is nearly coincident with the range of the periods exhibited by GD 358 for most of the range of possible effective temperatures. In particular, the pulsation periods of GD 358 fall into the highest excitation regimen (that is, shortest e -folding times), which reflects an

⁶ See Liddle (2004, 2007) for an equivalent formulation of the BIC index.

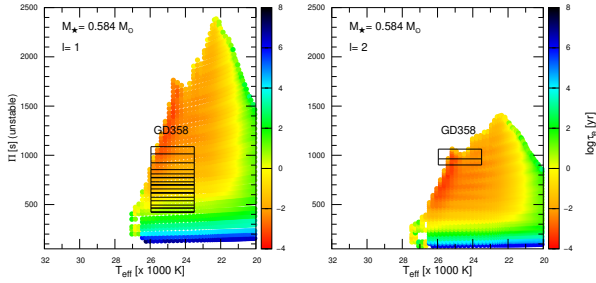


Fig. 9. Left panel: periods of excited $\ell = 1$ g modes as a function of the effective temperature, with the palette of colors (right scale) indicating the logarithm of the e -folding time (τ , in years), for the DB WD sequence with $M_\star = 0.584 M_\odot$. Right panel: same as left panel, but for $\ell = 2$ modes. In both panels, the pulsation periods of the DBV star GD 358, with the identification of ℓ according to our asteroseismological model (see Table 4), are shown as horizontal segments, where their widths represent the possible T_{eff} interval, according to spectroscopy.

excellent agreement between our nonadiabatic calculations and the observational data.

In Table 5, we list the main characteristics of GD 358 according to the previous studies and the present work. Most of the data of this table are extracted from Table 7 of Bischoff-Kim et al. (2019). In the case of the results of the present work, the errors in T_{eff} and $\log(L_\star/L_\odot)$ were estimated from the width of the maximum in the function $(\chi^2)^{-1}$ versus T_{eff} and $\log(L_\star/L_\odot)$, respectively, and the error in the stellar mass comes from the grid resolution in M_\star . Errors in the remainder quantities, $\log g$ and $\log(R_\star/R_\odot)$, were derived from these values. The seismological stellar mass ($0.584^{+0.025}_{-0.19} M_\odot$) is somewhat larger than the values derived from spectroscopy, although it is still compatible with them ($0.508 \pm 0.050 M_\odot$ and $0.560 \pm 0.028 M_\odot$) within their uncertainties. In addition, the stellar mass of the asteroseismological model is in excellent agreement with the stellar mass value derived from the mean period spacing ($0.588 \pm 0.024 M_\odot$). We can conclude that the three approaches to determine the stellar mass of GD 358 give very similar results, which implies that it is a well-constrained quantity.

In comparison with previous seismological studies, the effective temperature of our asteroseismological model is the largest one, although very similar to that derived by Fontaine & Brassard (2002), and in excellent agreement with the spectroscopic T_{eff} inferred by Bédard et al. (2017). Regarding the stellar mass of our asteroseismological model, its value is in excellent agreement with the values derived in all previous studies. Direct comparison of other quantities such as the central abundance of O (X_O), the thickness of the envelope rich in O, C, and He, $\log(1 - M_{\text{env}}/M_\star)$, or the thickness of the pure helium envelope, $\log(1 - M_{\text{He}}/M_\star)$, becomes less clear because the chemical structure of our DB WD models is (by construction) substantially different from those used in previous studies. Even so, we can note that the envelope of our asteroseismological model is somewhat thicker than in the previous studies, and that the pure-He envelope has a thickness quite similar to the thickness derived in other works.

We succinctly describe the main properties of our asteroseismological DB model for GD 358. We display in Fig. 10 the internal chemical profiles of this model (upper panel), where the abundance by mass of the main constituents (${}^4\text{He}$, ${}^{12}\text{C}$, and ${}^{16}\text{O}$) is depicted as a function of the outer mass fraction [$-\log(1 - M_r/M_\star)$]. The chemical structure of the model is char-

acterized by a C/O core –resulting from the core He-burning phase of the prior evolution– shaped by extra-mixing processes such as overshooting. The core is surrounded by a layer rich in He, C, and O, which results from the nucleosynthesis during the TP-AGB stage. Above this shell, there is a pure He mantle resulting from gravitational settling that causes He to float to the surface and heavier species to sink. The lower panel of Fig. 10 shows the squares of the two critical frequencies of nonradial stellar pulsations, that is, the Brunt-Väisälä frequency and the Lamb frequency L_ℓ for $\ell = 1$ and $\ell = 2$. The shape of the Brunt-Väisälä frequency largely defines the properties of the g-mode period spectrum of the model. In particular, each chemical transition region in the model contributes to the value of N locally. The most notable characteristic is the highly peaked structure at the C/O chemical transition [$-\log(1 - M_r/M_\star) \sim 0.34$]. On the other hand, there is the He/C/O interface at $-\log(1 - M_r/M_\star) \sim 1.3$ – 1.8 that causes the presence of a notable bump in the Brunt-Väisälä frequency and affects the mode-trapping properties of the model.

5.3. Asteroseismological distance

We can estimate an asteroseismological distance to GD 358 on the basis of the luminosity of the asteroseismological model [$\log(L_\star/L_\odot) = -1.215 \pm 0.015$ and $T_{\text{eff}} = 24967 \pm 200$ K] and a bolometric correction $BC = -2.71$ (Bradley & Winget 1994). The absolute magnitude can be assessed as $M_V = M_B - BC$, where $M_B = M_{B,\odot} - 2.5 \log(L_\star/L_\odot)$. We employed the solar bolometric magnitude $M_{B,\odot} = 4.74$ (Cox 2000). The seismological distance d was derived from the following relation: $\log d = [m_V - M_V + 5]/5$. We used the apparent visual magnitude $m_V = 13.65 \pm 0.01$ (Winget et al. 1982a), and obtained the seismological distance and parallax $d = 42.85 \pm 0.73$ pc and $\pi = 23.33 \pm 0.41$ mas. The uncertainty in the seismological distance comes from the uncertainty in the luminosity of the asteroseismological model. These values are consistent with the results of Bradley & Winget (1994) and Bischoff-Kim et al. (2019), although they are a bit larger than the distance derived by Bédard et al. (2017). A very important check for the validation of the asteroseismological model is the comparison of the seismological distance with the distance derived from astrometry. The estimates from Gaia EDR3, $d_G = 43.02 \pm 0.04$ pc and $\pi_G = 23.244 \pm 0.024$ mas, are available. They are in excellent agreement with the asteroseismological derivations. This adds robustness to the asteroseismological model we found for GD 358. Also, the match of seismological and trigonometric parallax confirm that we are seeing dipole modes.

6. Summary and conclusions

In this paper, we have presented new space observations of the already known DBV star GD 358. This is the first time that this star has been intensively examined by a space mission such TESS, which provides high-quality time-series photometry for asteroseismic purposes. The results of our analysis broadly confirm the previous observations from extensive ground-based observational campaigns. We also carried out a detailed asteroseismological analysis employing fully evolutionary models of DB WDs. We find that the evolutionary and pulsational properties of GD 358 according to our analysis based on space data combined with ground-based data are in line with the results of previous asteroseismological analyses of this star based on data from the ground alone. The present study is the third part of a series of papers devoted to the study of pulsating

Table 5. Main characteristics of the DBV star GD 358.

Quantity	Spectroscopy astrometry	BW94	DK95	MEA00	MEA01	FB02	M03	BKEA19	Seismology (this work)
T_{eff} [K]	$24\,000 \pm 500$ ^(a) $24\,937 \pm 1018$ ^(b)	24 000	24 121	22 600	22 600	24 800	22 900	23 650	$24\,967 \pm 200$
$\log g$ [cm s ⁻²]	7.78 ± 0.05 ^(a) 7.92 ± 0.05 ^(b)	8.0	8.02	$7.964^{+0.048}_{-0.043}$
M_{\star} [M_{\odot}]	0.508 ± 0.050 ^(c) 0.560 ± 0.028 ^(d)	0.61	0.58	0.605	0.65	0.625	0.66	0.571	$0.584^{+0.025}_{-0.019}$
$\log(L_{\star}/L_{\odot})$...	-1.30	-1.25	...	-1.287	-1.215 ± 0.015
$\log(R_{\star}/R_{\odot})$...	-1.90	-1.89	-1.880 ± 0.014
X_{O} (center)	...	0.50	0.50	0.80	0.84	0.00	0.67	0.50	0.77
$\log(1 - M_{\text{env}}/M_{\star})$	-2.6	-2.74	-2.74	-2.97	...	-2	-1.6
$\log(1 - M_{\text{He}}/M_{\star})$...	-5.70	-6.0	-5.97	...	-5.80	-2.0	-5.5	-5.98
d [pc]	36.6 ± 4.5 ^(b) 43.02 ± 0.04 ^(e)	42	43	...	44.5	42.85 ± 0.73

Notes. The second column corresponds to spectroscopic and astrometric results, whereas the third, fourth, fifth, sixth, seventh, and eighth columns present the results from the seismological studies of BW94 (Bradley & Winget 1994), DK95 (Dehner & Kawaler 1995), MEA00 (Metcalfe et al. 2000), MEA01 (Metcalfe et al. 2001), FB02 (Fontaine & Brassard 2002), M03 (Metcalfe 2003), and BKEA19 (Bischoff-Kim et al. 2019), respectively, and the last column presents the seismological results from the present work.

References. ^(a)Nitta et al. (2012); ^(b)Bédard et al. (2017); ^(c)From the evolutionary tracks and the T_{eff} and $\log g$ values of Nitta et al. (2012); ^(d)From the evolutionary tracks and the T_{eff} and $\log g$ values of Bédard et al. (2017); ^(e)Gaia.

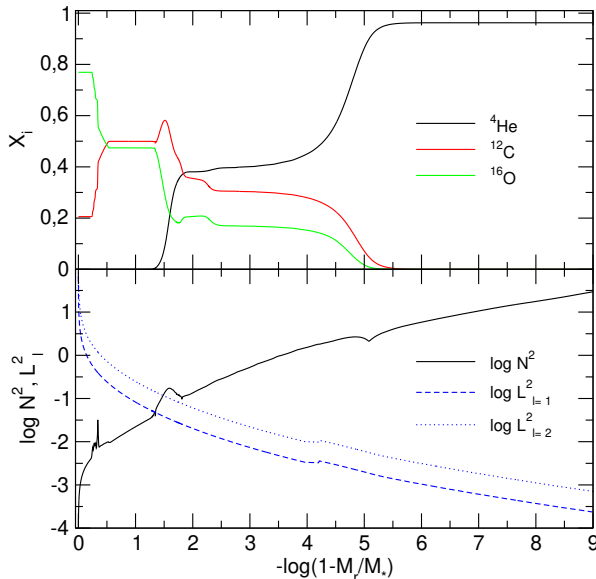


Fig. 10. Chemical profiles (upper panel) and the squared Brunt-Väisälä and Lamb frequencies for $\ell = 1$ and $\ell = 2$ (lower panel), corresponding to our asteroseismological DB WD model with a stellar mass $M_{\star} = 0.584 M_{\odot}$ and an effective temperature $T_{\text{eff}} = 24\,967$ K.

H-deficient WDs observed with TESS. We extracted 26 periodicities including eight combination frequencies from the TESS light curve of GD 358, using a standard pre-whitening procedure to derive the potential pulsation frequencies. The oscillation frequencies, associated with g -mode pulsations, have periods from ~ 422 s to ~ 1087 s. We combined these space data with the abundant ground-based observations available and found a constant period spacing of 39.25 ± 0.17 s, which allowed us to infer its stellar mass ($M_{\star} = 0.588 \pm 0.024 M_{\odot}$) and constrain the harmonic degree ℓ of some of the modes. We performed a period-to-period fit analysis on GD 358, which

provides us with an asteroseismological model with a stellar mass ($M_{\star} = 0.584^{+0.025}_{-0.019} M_{\odot}$) in agreement with the stellar-mass value inferred from the period spacing, and also compatible with the spectroscopic mass ($M_{\star} = 0.560 \pm 0.028 M_{\odot}$). In agreement with previous works, we found that the frequency splittings vary according to the radial order of the modes, suggesting differential rotation and preventing us from deriving a reliable and representative rotation period of the star. The seismological model derived from our analysis allowed us to estimate the seismological distance ($d_{\text{seis}} = 42.85 \pm 0.73$ pc) of GD 358, which is in excellent agreement with the precise astrometric distance measured by Gaia EDR3 ($d_{\text{Gaia}} = 43.02 \pm 0.04$ pc).

In accordance with the findings of our recent works focused on pulsating H-deficient WDs (Bell et al. 2019; Uzundag et al. 2021), we conclude that the high-quality data collected by the TESS space mission, combined with ground-based photometric data, are able to provide a reliable input to the asteroseismology of WD stars. The TESS mission, along with future space missions and upcoming surveys, will allow for an unprecedented boost to the stellar seismology of these ancient stars.

Acknowledgements. Part of this work was supported by AGENCIA through the Programa de Modernización Tecnológica BID 1728/OC-AR, and by the PIP 112-200801-00940 grant from CONICET. M. U. acknowledges financial support from CONICYT Doctorado Nacional in the form of grant number No: 21190886 and ESO studentship program. K. J. B. is supported by the National Science Foundation under Award AST-1903828. S. O. K. acknowledges financial support from Coordenação de Aperfeiçoamento de Pessoal de Nível Superior - Brasil (CAPES) – Finance Code 001, Conselho Nacional de Desenvolvimento Científico e Tecnológico – Brasil (CNPq), and Fundação de Amparo à Pesquisa do Rio Grande do Sul (FAPERGS) - Brasil. A. S. B. acknowledges financial support from the National Science Centre under projects No. UMO-2017/26/E/ST9/00703 and UMO-2017/25/B/ST9/02218. This research has made use of NASA's Astrophysics Data System. This paper includes data collected by the TESS mission. Funding for the TESS mission is provided by the NASA's Science Mission Directorate.

References

- Althaus, L. G., & Córscico, A. H. 2004, *A&A*, **417**, 1115
- Althaus, L. G., Córscico, A. H., Kepler, S. O., & Miller Bertolami, M. M. 2008, *A&A*, **478**, 175
- Althaus, L. G., Panei, J. A., Miller Bertolami, M. M., et al. 2009, *ApJ*, **704**, 1605

- Althaus, L. G., Córscico, A. H., Isern, J., & García-Berro, E. 2010, *A&ARv*, **18**, 471
- Bailer-Jones, C. A. L., Rybizki, J., Fouesneau, M., Demleitner, M., & Andrae, R. 2021, *VizieR Online Data Catalog*, **1/352**
- Baran, A. S., & Koen, C. 2021, *Acta Astron.*, **71**, 113
- Bédard, A., Bergeron, P., & Fontaine, G. 2017, *ApJ*, **848**, 11
- Bell, K. J. 2017, PhD Thesis, University of Texas, USA
- Bell, K. J., Hermes, J. J., Bischoff-Kim, A., et al. 2015, *ApJ*, **809**, 14
- Bell, K. J., Hermes, J. J., Vanderbosch, Z., et al. 2017, *ApJ*, **851**, 24
- Bell, K. J., Córscico, A. H., Bischoff-Kim, A., et al. 2019, *A&A*, **632**, A42
- Bischoff-Kim, A., & Østensen, R. H. 2011, *ApJ*, **742**, L16
- Bischoff-Kim, A., Østensen, R. H., Hermes, J. J., & Provencal, J. L. 2014, *ApJ*, **794**, 39
- Bischoff-Kim, A., Provencal, J. L., Bradley, P. A., et al. 2019, *ApJ*, **871**, 13
- Bognár, Z., Paparó, M., Córscico, A. H., Kepler, S. O., & Győrffy, A. 2014, *A&A*, **570**, A116
- Bohm, K. H., & Cassinelli, J. 1971, *A&A*, **12**, 21
- Borucki, W. J., Koch, D., Basri, G., et al. 2010, *Science*, **327**, 977
- Bradley, P. A., & Winget, D. E. 1994, *ApJ*, **430**, 850
- Bradley, P. A., Winget, D. E., & Wood, M. A. 1993, *ApJ*, **406**, 661
- Brassard, P., Fontaine, G., Wesemael, F., & Hansen, C. J. 1992, *ApJS*, **80**, 369
- Brickhill, A. J. 1991, *MNRAS*, **251**, 673
- Castanheira, B. C., Nitta, A., Kepler, S. O., Winget, D. E., & Koester, D. 2005, *A&A*, **432**, 175
- Charpinet, S., Brassard, P., Giannicchele, N., & Fontaine, G. 2019, *A&A*, **628**, L2
- Córscico, A. H., & Althaus, L. G. 2006, *A&A*, **454**, 863
- Córscico, A. H., Althaus, L. G., Benvenuto, O. G., & Serenelli, A. M. 2002, *A&A*, **387**, 531
- Córscico, A. H., Althaus, L. G., & Miller Bertolami, M. M. 2006, *A&A*, **458**, 259
- Córscico, A. H., Althaus, L. G., Miller Bertolami, M. M., & García-Berro, E. 2009, *J. Phys. Conf. Ser.*, **172**, 012075
- Córscico, A. H., Althaus, L. G., Kawaler, S. D., et al. 2011, *MNRAS*, **418**, 2519
- Córscico, A. H., Althaus, L. G., Miller Bertolami, M. M., & Bischoff-Kim, A. 2012, *A&A*, **541**, A42
- Córscico, A. H., Althaus, L. G., Miller Bertolami, M. M., Kepler, S. O., & García-Berro, E. 2014, *JCAP*, **8**, 054
- Córscico, A. H., Althaus, L. G., Miller Bertolami, M. M., & Kepler, S. O. 2019, *A&ARv*, **27**, 7
- Córscico, A. H., Uzundag, M., Kepler, S. O., et al. 2021, *A&A*, **645**, A117
- Cox, A. N. 2000, Allen's Astrophysical Quantities
- Dehner, B. T., & Kawaler, S. D. 1995, *ApJ*, **445**, L141
- Duan, R. M., Zong, W., Fu, J. N., et al. 2021, *ApJ*, **922**, 2
- Dupret, M. A., Quirion, P. O., Fontaine, G., Brassard, P., & Grigahcène, A. 2008, *J. Phys. Conf. Ser.*, **118**, 012051
- Fontaine, G., & Brassard, P. 2002, *ApJ*, **581**, L33
- Fontaine, G., & Brassard, P. 2008, *PASP*, **120**, 1043
- Giannicchele, N., Charpinet, S., Fontaine, G., et al. 2018, *Nature*, **554**, 73
- Goldreich, P., & Wu, Y. 1999, *ApJ*, **511**, 904
- Greiss, S., Gänsicke, B. T., Hermes, J. J., et al. 2014, *MNRAS*, **438**, 3086
- Hermes, J. J., Gänsicke, B. T., Kawaler, S. D., et al. 2017a, *ApJS*, **232**, 23
- Hermes, J. J., Kawaler, S. D., Bischoff-Kim, A., et al. 2017b, *ApJ*, **835**, 277
- Howell, S. B., Sobeck, C., Haas, M., et al. 2014, *PASP*, **126**, 398
- Kawaler, S. D. 1988, in Advances in Helio- and Asteroseismology, eds. J. Christensen-Dalsgaard, & S. Frandsen, *IAU Symp.*, **123**, 329
- Kawaler, S. D., & Bradley, P. A. 1994, *ApJ*, **427**, 415
- Kawaler, S. D., Sekii, T., & Gough, D. 1999, *ApJ*, **516**, 349
- Kepler, S. O. 1993, *Balt. Astron.*, **2**, 515
- Kepler, S. O., Nather, R. E., Winget, D. E., et al. 2003, *A&A*, **401**, 639
- Kepler, S. O., Pelisoli, I., Koester, D., et al. 2015, *MNRAS*, **446**, 4078
- Kepler, S. O., Pelisoli, I., Koester, D., et al. 2016, *MNRAS*, **455**, 3413
- Kepler, S. O., Pelisoli, I., Koester, D., et al. 2019, *MNRAS*, **486**, 2169
- Kleinman, S. J., Nather, R. E., Winget, D. E., et al. 1998, *ApJ*, **495**, 424
- Kleinman, S. J., Kepler, S. O., Koester, D., et al. 2013, *ApJS*, **204**, 5
- Koen, C., & Laney, D. 2000, *MNRAS*, **311**, 636
- Koester, D., Provencal, J., & Gänsicke, B. T. 2014, *A&A*, **568**, A118
- Kong, X., & Luo, A.-L. 2021, *Res. Notes AAS*, **5**, 249
- Landolt, A. U. 1968, *ApJ*, **153**, 151
- Ledoux, P., & Walraven, T. 1958, *Handbuch der Physik*, **51**, 353
- Liddle, A. R. 2004, *MNRAS*, **351**, L49
- Liddle, A. R. 2007, *MNRAS*, **377**, L74
- Metcalfe, T. S. 2003, *ApJ*, **587**, L43
- Metcalfe, T. S., Nather, R. E., & Winget, D. E. 2000, *ApJ*, **545**, 974
- Metcalfe, T. S., Winget, D. E., & Charbonneau, P. 2001, *ApJ*, **557**, 1021
- Montgomery, M. H., Hermes, J. J., Winget, D. E., Dunlap, B. H., & Bell, K. J. 2020, *ApJ*, **890**, 11
- Mukadam, A. S., Mullally, F., Nather, R. E., et al. 2004a, *ApJ*, **607**, 982
- Mukadam, A. S., Winget, D. E., von Hippel, T., et al. 2004b, *ApJ*, **612**, 1052
- Mukadam, A. S., Montgomery, M. H., Winget, D. E., Kepler, S. O., & Clemens, J. C. 2006, *ApJ*, **640**, 956
- Nather, R. E., Winget, D. E., Clemens, J. C., Hansen, C. J., & Hine, B. P. 1990, *ApJ*, **361**, 309
- Nitta, A., Koester, D., Chu, D., et al. 2012, in Progress in Solar/Stellar Physics with Helio- and Asteroseismology, eds. H. Shibahashi, M. Takata, A. E. Lynas-Gray, et al., *ASP Conf. Ser.*, **462**, 171
- O'Donoghue, D. 1994, *MNRAS*, **270**, 222
- Østensen, R. H., Bloemen, S., Vučković, M., et al. 2011, *ApJ*, **736**, L39
- Provencal, J. L., Montgomery, M. H., Kanaan, A., et al. 2009, *ApJ*, **693**, 564
- Quirion, P. O., Dupret, M. A., Fontaine, G., Brassard, P., & Grigahcène, A. 2008, in Hydrogen-Deficient Stars, eds. A. Werner, & T. Rauch, *ASP Conf. Ser.*, **391**, 183
- Ricker, G. R., Winn, J. N., Vanderspek, R., et al. 2015, *J. Astron. Telesc. Instrum. Syst.*, **1**, 014003
- Tassoul, M. 1980, *ApJs*, **43**, 469
- Tassoul, M., Fontaine, G., & Winget, D. E. 1990, *ApJs*, **72**, 335
- Unno, W., Osaki, Y., Ando, H., Saio, H., & Shibahashi, H. 1989, Nonradial Oscillations of Stars
- Uzundag, M., Córscico, A. H., Kepler, S. O., et al. 2021, *A&A*, **655**, A27
- Van Grootel, V., Fontaine, G., Brassard, P., & Dupret, M. A. 2017, in 20th European White Dwarf Workshop, eds. P. E. Tremblay, B. Gaensicke, & T. Marsh, *ASP Conf. Ser.*, **509**, 321
- Vuille, F., O'Donoghue, D., Buckley, D. A. H., et al. 2000, *MNRAS*, **314**, 689
- Winget, D. E., & Kepler, S. O. 2008, *ARA&A*, **46**, 157
- Winget, D. E., van Horn, H. M., Tassoul, M., et al. 1982a, *ApJ*, **252**, L65
- Winget, D. E., Robinson, E. L., Nather, R. D., & Fontaine, G. 1982b, *ApJ*, **262**, L11
- Winget, D. E., van Horn, H. M., Tassoul, M., Hansen, C. J., & Fontaine, G. 1983a, *ApJ*, **268**, L33
- Winget, D. E., Hansen, C. J., & van Horn, H. M. 1983b, *Nature*, **303**, 781
- Winget, D. E., Nather, R. E., Clemens, J. C., et al. 1994, *ApJ*, **430**, 839
- Wu, Y., & Goldreich, P. 1999, *ApJ*, **519**, 783
- York, D. G., Adelman, J., Anderson, J. E., Jr, et al. 2000, *AJ*, **120**, 1579